

# A New Experimental Model of Krypton Laser-Induced Choroidal Neovascularization in Tree Shrew

Xiao-Chen LIU

Southern Central Hospital of Yunnan Province, The First people's Hospital of Honghe State

Min WU (✉ [ynwumin@126.com](mailto:ynwumin@126.com))

The Affiliated Hospital of Yunnan University (The 2nd People's Hospital of Yunnan Province) Yunnan Eye Disease Clinical Medical Center Yunnan

---

## Article

**Keywords:** Tree Shrew, laser, CNV model, angiogenesis-related factors

**Posted Date:** March 25th, 2022

**DOI:** <https://doi.org/10.21203/rs.3.rs-1454150/v1>

**License:**  This work is licensed under a Creative Commons Attribution 4.0 International License. [Read Full License](#)

---

## Abstract

## Purpose

This study was designed to establish a new choroidal neovascularization (CNV) model on tree shrew, and evaluate whether it is an ideal experimental animal model for CNV-related research.

## Methods

60 tree shrews (60 eyes) were divided into one normal group and five experimental groups. Krypton laser photocoagulation was applied for CNV induction on tree shrew. Fundus fluorescein angiography (FFA), indocyanine green angiography (ICGA), spectral-domain optical coherence tomography (SD-OCT) and flash visual evoked potential (F-VEP) were examined at 3, 7, 14, 21, and 28 days after laser. The pathological performance was observed by pathological section. The expression of multiple angiogenesis-related factors during CNV formation were checked by quantitative real-time polymerase chain reaction (qRT-PCR).

## Results

According to FFA and ICGA findings, success rate of CNV modeling on tree shrew was 70%. OCT showed the formation of typical CNV lesions on tree shrew. F-VEP indicated characteristic decrease of N1-P1 wave amplitude after CNV development. Pathological examination showed thin-walled new blood vessels emerging from choroid. The significant increased/decreased expression of angiogenesis-related factors were detected by qRT-PCR.

## Conclusions

Krypton laser photocoagulation can successfully induce the CNV model on tree shrew with high success rate. The tree shrew CNV model could be widely accessible to CNV-related research.

## Introduction

Choroidal neovascularization (CNV) is a common pathological change of multiple ocular fundus disease, such as age-related macular degeneration (AMD)<sup>1</sup>, pathologic myopia<sup>2</sup>, angioid streaks, and ocular histoplasmosis syndrome<sup>3</sup>. The pathological mechanism manifests as new blood vessels arising from the choroid sprout into the sub-retinal pigment epithelial (RPE) space, gradually extend to the subretinal area or into neural retina. CNV in macular area may cause macular hemorrhage and subretinal exudation<sup>4–6</sup>. In FFA examinations, active CNV lesion mainly showed as the fluorescein leakage at early stage and fluorescein staining at late stage, with peripheral hemorrhage and exudation<sup>7</sup>. The fibrotic scar formation in macular area could be seen at the terminal stage of disease, eventually leading to the irreversible blindness. Nowadays, CNV-related ophthalmopathy has become one of the major causes of blindness in the world<sup>8</sup>.

In 1981, two essential conditions for CNV formation were proposed by Archer et al: the rupture of Bruch membrane and the structural changes of outer retinal layer<sup>9</sup>. Based on the above theory, Archer et al successfully established the laser-induced CNV model on Rhesus<sup>9</sup>. At present, laser treatment has become one of the most common and mature methods for CNV modeling. During laser photocoagulation, photoreceptor outer segments, RPE layer, Bruch membrane and choriocapillary layer could be selectively destructed, which in turn triggers a series of repair processes and new blood vessel formation<sup>10</sup>. Laser induced models of CNV have been created on rat, mouse, rabbit, pig, and primate successfully so far<sup>11–13</sup>.

The Chinese tree shrew (*Tupaia belangeri*) currently placed in the order of Scandentia, is a small mammal weighs 100–150g, with short reproductive and life cycles, high reproductivity (4–6 months from birth to adulthood, with 2–6 offspring born each time), and has a wide distribution in Southeast Asia and South and Southwest China<sup>14,15</sup>. In recent years, numerous tree shrew models have been generated in biological and medical studies, including research on virus infection, bacterial infection, immune-related disease, cancer, metabolic disease, mental disease, and nerve related diseases<sup>15</sup>. Tree shrew has been also used in researches of eye diseases frequently, such as myopia, visual dysplasia, and amblyopia<sup>16,17</sup>. Due to the complex and still unclear pathogenesis of CNV, the laser induced CNV model has been applied in all aspects of CNV-related investigations. The purpose of this research was to establish laser-induced CNV model on tree shrew, aimed to explore the similarities between tree shrew CNV and human CNV disease from multiple aspects, including clinical and morphological manifestations, the expression of various of angiogenesis-related factors during CNV formation were also detected. In this research, CNV was established in a new kind of animal model, which could be widely applied to CNV-related research, such as leading to a deeper understanding of pathogenesis and morphology of CNV, as well as studying the molecular mechanisms driving angiogenesis, in order to develop novel therapies. Finally, this new animal model could be also used in studies involving pharmacological and toxicological evaluation, assessing new treatment modalities including intravitreal injection of anti-angiogenic agents, which is vital for developing new treatment method in the future.

## Material And Methods

### Animals

sixty healthy Chinese tree shrews aged 2–3 years and weighing 150g–200g were purchased from the Center of Tree Shrew Germplasm Resources, Institute of Medical Biology, Chinese Academy of Medical Sciences, Peking Union Medical College (Kunming, China). Slit-lamp and indirect ophthalmoscopy examination were performed to exclude animals with any ocular disease. All the tree shrews in this study were settled and treated according to the ARRIVE (Animal

Research: Reporting of In Vivo Experiments) guidelines. The experimental process was approved by the Ethical Committee for Animal Research in The Affiliated Hospital of Yunnan University.

According to whether photocoagulation was performed and the observation time point after photocoagulation, 60 tree shrews (60 eyes) were divided into one normal group (10 eyes of 10 healthy tree shrews) and the following five experimental groups. Group 3 days (G3D): 3 days after photocoagulation, Group 7 days (G7D): 7 days after photocoagulation, Group 14 days (G14D): 14 days after photocoagulation, Group 21 days (G21D): 21 days after photocoagulation, Group 28 days (G28D): 28 days after photocoagulation. Each experimental group contained 10 animals (10 eyes). All the laboratory animals for this research were raised on the Center of Tree Shrew Germplasm Resources before and post laser or other examinations.

## Laser-induced Cnv

All the tree shrews in experimental groups were anesthetized by intraperitoneal injections with pentobarbital sodium (4.5 mg/kg, sigma, USA). Pupils were dilated with 0.5% tropicamide (Santen, Osaka, Japan). Laser spots were applied around the optic disc on the left eye of each animal. Multi-wavelength laser machine (Lumenis, USA) was used for photocoagulation. The parameter settings are as follows: select the krypton laser mode, wavelength: 647nm, spot size: 50 $\mu$ m, duration: 0.05s, laser energy: 350 mw. The appearance of plosive and bubble-like change during photocoagulation indicates the rupture of Bruch membrane. Ocular fundus photographs were obtained by non-mydratic fundus photography (NIDEK, Japan), immediately after photocoagulation.

## Fundus Fluorescein Angiography And Indocyanine Green Angiography

Fundus fluorescein and indocyanine green angiography were performed on different experimental groups at 3 days, 7 days, 14 days, 21 days, 28 days after photocoagulation respectively. The same examinations were also performed on normal group. Tree shrews were anesthetized with intraperitoneal pentobarbital sodium (4.5 mg/kg), then, 10% sodium fluorescein and 1.25% indocyanine green were mixed by 1:1 ratio, and the mixture was injected via tail vein at 0.2ml/kg. The late-phase angiograms were obtained at 15min after injection. Simultaneous appearance of fluorescence leakage in FFA and mottled strong fluorescence in ICGA was considered as CNV formation. According to FFA and ICGA findings, the success rate of CNV modeling were calculated. The success rate of CNV modeling was defined as the percentage of CNV formation spots in the total laser spots.

## Spectral-domain Optical Coherence Tomography (Sd-oct)

SD-OCT was used to evaluate the morphological characteristics of tree shrew CNV. OCT image of different experimental groups were obtained at 3 days, 7 days, 14 days, 21 days, 28 days after photocoagulation respectively. OCT image of normal group was also acquired. The examination was performed under deep anesthesia. All the images were obtained by the same SD-OCT machine (OCT SPECTRALIS, Germany, Heiderberg Engineering GmbH 69121) by the same technician. Each laser spot was scanned horizontally under linear scan mode. The parameter settings are as follows: scan wavelength: 820nm, scan depth: 2.0mm, scan speed :27000 A/s, length of scanning line: 3mm, lateral resolution: 20 $\mu$ m. One hundred scanning were performed at each laser spot. Superposition images were acquired.

## Flash Visual Evoked Potential (F-vep)

F-VEP examination for all the experimental animals was performed before photocoagulation, and the F-VEP characteristics of healthy tree shrews were obtained. Then, the same examination was performed on different experimental groups at 3 days, 7 days, 14 days, 21 days, 28 days after photocoagulation respectively. F-VEP images, and their corresponding amplitudes and latency of each wave were recorded. The examination was performed under deep anesthesia. All the images were obtained by the using of visual electric physiological system (IRC, China). The parameter settings are as follows: stimulated by full field white flash, flash intensity: 3cd/m<sup>2</sup>/s, passband range: 1-75Hz, superimposed for 64 times, magnification: 20,000, coordinate time: 25ms/d, longitudinal depiction: 10 $\mu$ v/d, longitudinal depiction of real-time signal: 100 $\mu$ v/d.

## Histological Examination

Animals from different experimental groups were sacrificed by excessive anesthesia with intraperitoneal injections of pentobarbital sodium (13.5mg/kg) at 3 days, 7 days, 14 days, 21 days, 28 days after laser treatment respectively, and the whole eyeballs were collected. The eyeballs of normal group were also removed. To fix the tissue rapidly, 4% formaldehyde phosphate buffered was injected into the vitreous cavity until the eyeballs were plumped, then the eyeballs were transferred into the same stationary liquid for 24 hours. The cornea, lens, iris and vitreous body were removed from the eyeball, and the posterior ocular wall tissue was retained. The fixed and dehydrated tissue was embedded in paraffin. Paraffin sections of 5 $\mu$ m thickness were cut, and serial sections were collected when the first lesion was identified. Hematoxylin-eosin staining was performed. The relative thickness of CNV membrane was estimated by the ratio (B/C) of the thickness from the bottom of the pigmented choroidal layer to the top of the neovascular membrane (B) to the thickness of the intact pigmented choroid adjacent to the lesion (C), according o Lambert et al<sup>18</sup>. The thickness was measured by Image pro plus 6.0 (MEDIA CYBERNETICS, USA).

## Qrt-pcr Analysis

## Purification of RNA, cDNA synthesis

After removal of eyeballs, the choroid tissue was dissected and immediately frozen in liquid nitrogen. The frozen tissues were first pulverized using glass homogenizer, and total RNA was extracted with the EastepTMSuper Total RNA Extraction Kit (Promega:LS1040, USA) according to the manufacturer's protocol. RNA integrity was evaluated by the 18S and 28S rRNA bands in 1.5% ethidium bromide–stained agarose gels. Concentration of total RNA was quantified by the determination of optical density at 260nm (OD260), total RNA was used for reverse transcription. Reverse transcription (RT) system including 4µl of Goscript™ Reaction Buffer Oligo (dT), 2µl of Goscript™ Enzyme Mix (Promega: A2790), and 14µl of RNA template. RT was performed according to the manufacturer's protocol. Finally, tubes were incubated for 20min at 42°C, heated to 90°C for 5 min. Samples were stored at -20°C until further use.

## Sybr Green I Real-time Pcr

For real-time PCR amplification, the reaction mixture (25µL) contained 2µl of template cDNA, 1µl of each primer set, 12.5µL of Power SYBR Green PCR Master mix (Applied Biosystems), 8µL of nuclease-free water, and 0.5µL of ROX. Reactions were performed using the Applied Biosystems 7300 Real-Time PCR System, with the following PCR conditions: 50°C for 2 min, 95°C for 10 min, followed by 95°C for 15 s and 60°C for 1 min, repeated for 40 cycles. Tm curve analysis was performed using SDS software 1.2 (Applied Biosystems). The sequences of sense and antisense primers used in this study are shown in Table 1.

Table 1  
Primer sequences

Gene name	Forward primer	Reverse primer
GAPDH	AGGAGTGGGTGTCGCTGTTGA	TGACCTGCCGCTGGAGAAAG
VEGF-A	TTCTTTGGTCTGCATTCACAT	CACCGAGGAGTTCAACATCAC
VEGF-B	TGTAGGAGACTTTGAACTTGC	AGACTGTAAAAGGTGTCATCA
Ang-1	ACTGTTGTTGGTGGTGGCTCT	CTTCAAGGCTTGGTTACTCGT
Ang-2	CCAGTATTCTCCTGAAGGGTT	GTGAAGATGGCAGTGTGATT
bFGF	CACGGTTGGGTTTGCCTTGT	ACTCTGGGGTTCTGCTGGTTC
TGF-β	AGGGTTGGGGTGGCTTCGTCC	CCCGTGTCCGTGCCTTACTCA
PEDF	GGTCCATAAGACTTTTCCAG	CAGACATCCACAGCACCTACA
MMP2	CAGTGTC AATGTCAGGGGAGG	CTACGATGATGACCGCAAGTG
MMP9	CGATCTTGGCAGAAGTAGGCT	CGTGAAAACGCAGAAGGTGGA
MMP13	TCGCCTCGGAGACTGGTAATG	GGAGATGAAGACCCCAACCCT
PIGF	AATGTCTCCAACCAACTCT	TTTTGTAAGTCTGTCAACCT

## Statistical analysis

All the statistical analyses were performed using SPSS version 17.0 for Windows (Inc., Chicago, IL, USA). The comparison of B/C values, and the relative expression of various factors among multiple groups were analyzed by ANOVA (analysis of variance). Further comparison between each experimental group and normal group was performed by LSD-t test. The difference of amplitude and latency between each experimental group and normal group in F-VEP examination were compared with paired-samples t test. Statistical significance was defined as  $P < 0.05$ .

## Results

### Fundus photography before and after photocoagulation

Retina images of healthy tree shrew appears as orange reflection. Elliptical optic disk could also be seen at the posterior pole, with several radial blood vessels emitted. Arteries and veins distributed on the retina are clearly visible. Tree shrews have no macula lutea. Laser photocoagulation is carried out with laser spots that are approximately 1 disc in diameter away from the optic disk. Formation of an acute bubble indicates the successful rupture of Bruch's membrane<sup>19</sup>, some spots are accompanied with few choroidal hemorrhage beneath the retina (Fig. 1).

### The Ffa/icga Performance And Modeling Success Rate

After the injection of fluorescein sodium and indocyanine green mixed solution, the simultaneous angioplerosis of retinal arteries and veins in healthy tree shrews could be observed by FFA examination, the evenly distributed background fluorescence in choroid could also be seen. The angioplerosis of choroidal vessels could also be seen in ICGA (Fig. 2). At 3 days after photocoagulation, FFA showed that pieces of low background fluorescence presented at laser spot, ICGA showed the clumpy of high fluorescence in the corresponding position. At 7–21 days after photocoagulation, the mottled strong fluorescence appeared in ICGA images, while FFA showed strong fluorescence with fluorescein leakage. At the late stage of angiography, the leakage boundary expanded and surrounding tissue was stained. At 28 days after photocoagulation, strong fluorescence in ICGA disappeared, leaving sheet of low fluorescence behind. While FFA showed fluorescence leakage vanished, leaving the scar tissue dyed (Fig. 3). The success rate of CNV modeling and the total area of fluorescent leakage in both eyes are shown in Table 2.

Table 2  
The success rate of CNV modeling and the total area of fluorescent leakage

Time duration after photocoagulation	Number of CNV lesions of living tree shrews(Number of laser spots)	The success rate of CNV modeling (%)	The total area of fluorescent leakage(mm <sup>2</sup> ) $\bar{x}\pm SD$
3 days	0(400)	0.0	—
7 days	147(320)	46.0	2.99 $\pm$ 1.21
14 days	120(240)	50.0	6.46 $\pm$ 2.74
21 days	112(160)	70.0	10.25 $\pm$ 6.39
28 days	9(80)	11.3	1.55 $\pm$ 0.31

## Tree Shrew Cnv Detected By Sd-oct

The anatomical structure of retina and choroid in healthy tree shrew could be showed clearly in SD-OCT scan. The posterior segment performance of healthy tree shrew in SD-OCT was similar to human. In SD-OCT examination, strong reflection manifestation includes retinal nerve fiber layer, photoreceptor layer, and RPE-choriocapillaris complex. Medium reflection includes inner and outer plexiform layers. Weak reflection includes inner and outer nuclear layers (Fig. 4). After laser photocoagulation, laser spots were displayed by red-free fundus photography distinctly (Fig. 5). At 3 days after photocoagulation, the break of RPE connection, thickening and deformation of RPE and choroidal capillaries was confirmed by SD-OCT examination. At day 7, irregular incassation and rupture of RPE and choroid was observed, with the formation of spindle-shaped, high-reflection region upward the RPE layer. At 14 days after photocoagulation, the breadth and height of high-reflection region increased. At 21–28 days after photocoagulation, the breadth and height of the lesion were similar to 14 days group, but scar reflection of retina, RPE and choroid were observed, and aggravated with the extension of modeling time (Fig. 6).

## F-vep Variation Induced By Cnv

The NPN is the main waveform of healthy tree shrew in F-VEP. Which is consists of large-amplitude N1-P1-N2 and post waves including P2, N3, and P3. The F-VEP waveform of tree shrew is relatively stable. Similar waveforms were revealed in both eyes of the same animal. However, there are significant differences in amplitude among different individuals (Fig. 7). VEP index values for healthy tree shrew were showed in Table 2. Compared with tree shrew before photocoagulation, amplitudes of N1-P1 decreased significantly in each experimental group. As for the rest waveforms, the amplitude was varied in different groups. There is no common waveform with prolonged latency among different experimental groups. Index values of F-VEP after photocoagulation and statistical analysis were showed in Table 3 and Fig. 8.

Table 3  
VEP index values for healthy tree shrew(mean ± SD)

Item	Sample number	3 days before photocoagulation	3 days after photocoagulation	7 days before photocoagulation	7 days after photocoagulation	14 days before photocoagulation	14 days after photocoagulation	21 days after photocoagulation
Latency of N1 wave(ms)	10	39.00 ± 10.64	34.95 ± 9.04	34.26 ± 12.08	35.55 ± 15.61	35.00 ± 11.07	36.20 ± 13.81	44.6
Latency of P1 wave(ms)	10	62.10 ± 9.89	54.81 ± 11.38	56.60 ± 5.07	54.05 ± 16.80	50.60 ± 14.06	52.05 ± 12.01	60.5
Latency of N2 wave(ms)	10	79.40 ± 9.42	70.75 ± 9.98	72.20 ± 13.75	75.65 ± 5.46	72.20 ± 13.75	75.65 ± 5.46	79.3
Latency of P2 wave(ms)	10	109.35 ± 13.79	123.85 ± 16.80***	114.70 ± 26.14	102.05 ± 23.20	87.85 ± 20.98	109.20 ± 17.55*	105.1
Latency of N3 wave(ms)	10	134.75 ± 25.06	148.60 ± 33.44	141.20 ± 33.22	131.35 ± 13.66	131.40 ± 23.52	165.40 ± 28.85*	153.1
Latency of P3 wave(ms)	10	209.80 ± 40.43	223.90 ± 27.65	209.95 ± 28.36	225.45 ± 22.18*	215.45 ± 24.86	211.80 ± 32.20	207.1
Amplitude of N1-P1(μv)	10	15.92 ± 6.47	9.89 ± 5.44*	18.61 ± 6.98	12.17 ± 7.59**	14.47 ± 4.72	8.45 ± 3.06***	20.6
Amplitude of N2-P2(μv)	10	14.36 ± 6.72	7.63 ± 3.85*	13.06 ± 7.55	14.79 ± 8.37	7.44 ± 4.20	7.59 ± 3.58	22.2
Amplitude of N3-P3(μv)	10	18.17 ± 13.56	8.28 ± 9.12	11.95 ± 8.10	12.79 ± 5.12	18.93 ± 4.72	5.95 ± 2.82**	13.5

\*means  $P < 0.05$ , \*\*means  $P < 0.01$ , \*\*\*means  $P < 0.001$

## Pathological Section Of Healthy Tree Shrew And Tree Shrew Cnv

The structure of posterior eyeball wall of healthy tree shrew was clearly showed in pathological sections. The sclera is mainly composed by fibrous tissue. The choroid is constituted by connective tissue, containing large number of blood vessels. Structures of each layer of retina were also displayed in the section. The composition and arrangement of posterior segment in tree shrews resembled those of human (Fig. 9). Comparing with the normal group, the complete fracture of retina from inner nuclear layer to RPE layer could be seen in 3 days group. Choroidal capillary layers were broken and choroidal pigment cells invaded into retina tissue from the breaking point. No neovascularization was observed. At day 7, the infiltration of pigment cells was more obvious. New capillaries emerged from choroid, which had grown into or underneath the retina through the rupture position of Bruch membrane. At day 14, the density and height of neovessels increased significantly. At day 21–28, neovessels were existing stably (Fig. 10). At higher magnification, the newly formed thin-walled capillaries could be seen, with red blood cells in the lumen. In addition, the infiltration of pigment cell, pigmentary macrophage and small lymphocyte were also noticed in the CNV area (Fig. 11). According to the findings from quantification analysis, the B/C value in each experimental group was significantly higher than normal group ( $P < 0.05$ ), and the relative height of CNV lesion peaked at 14 days after photocoagulation (Fig. 12). According to the observation of pathological section, CNV formed at 7 days after photocoagulation, the relative height of neovessels peaked at day 14.

## Relative Expression Of Angiogenesis-related Factors In Tree Shrew Choroid

Based on findings from qRT-PCR and statistical analysis, the relative expression of 11 angiogenesis-related factors in experimental groups changed to various degrees. Compared with the normal group, the expression of vascular endothelial growth factor-A (VEGF-A) mRNA increased significantly at day 3 and day 14–28 ( $P < 0.05$ ). The expression of VEGF-B mRNA increased significantly and reached its peak at day 3 ( $P < 0.05$ ). The expression of angiopoietin-1 (ANG-1) mRNA increased significantly from 7 to 28 days after photocoagulation ( $P < 0.05$ ). The expression of Ang-2 mRNA increased significantly at day 3, 7, 14 and day 28 ( $P < 0.05$ ). The expression of matrix Metalloproteinases-2(MMP-2) mRNA decreased significantly at 14–21 days after photocoagulation ( $P < 0.05$ ). The expression of MMP-9 mRNA increased significantly and peaked at day 3 ( $P < 0.05$ ). The expression of MMP-13 mRNA significantly increased at day 3–7 ( $P < 0.05$ ), and reached its peak at day 7. The expression of basic fibroblast growth factor(bFGF) mRNA increased significantly at day 7, 14 and day 28 ( $P < 0.05$ ). The expression of placental growth factor (PLGF) mRNA peaked at 3 days after photocoagulation ( $P < 0.05$ ), and decreased slightly from day 7 to day 28, but still significantly higher than normal group ( $P < 0.05$ ). The expression of TGF-β mRNA significantly decreased from 7 days to 21 days after photocoagulation

( $P < 0.05$ ), and reached the lowest at day 21. The expression of Pigment Epithelium Derived Factor (PEDF) mRNA decreased significantly from 3 days to 28 days after photocoagulation ( $P < 0.05$ ). The expression trend of various angiogenesis-related factors was shown in the Fig. 12, 13.

## Discussion

Nowadays, the way of CNV modeling mainly composed of surgery, genetic modification, and laser photocoagulation based on different theories. However, the relative importance of mechanical injury to Bruchs membrane, VEGF production, and inflammatory cytokine mediation during CNV formation on various animal CNV model may be aware of. Surgery induced CNV models are mainly based on subretinal introduction of VEGF or inflammatory cytokine aggregation<sup>20</sup>, there are also a few surgery induced CNV based on mechanical perforation of subretinal Bruch membrane or penetrating retinal injury, which may induce and promote the pathological choroidal neovascularization<sup>13</sup>. Rabbit CNV model were induced by the over expression of angiogenic factors such as VEGF/bFGF, which were conducted by injection or implantation of VEGF/bFGF in the suprachoroidal/subretinal space<sup>21-24</sup>. In rat CNV model induced by subretinal injection of an adeno-associated virus (AAV) -VEGFA165 vector, CNV area reaches a peak at six weeks after VEGF transduction, which was observed in 93% of the eyes<sup>25</sup>. Transgenic mouse model with subretinal injection of human VEGF-A165 by adenoviral Cre gene delivery showed the maximal CNV areas in angiography at two weeks after the subretinal injection in 75% of the total mice, and the CNV area began to diminish at later time points<sup>26</sup>. In another less commonly used rats CNV model induced by subretinal matrigel injection, CNV was observed at 4 days after injection and increased in size progressively, and continued into 20 days after injection<sup>27</sup>. The principal mechanism of CNV development on transgenic animals are RPE oxidative damage, RPE abnormalities, retinal lesions, defects in Bruchs membrane, and over-expressing of angiogenic factors including VEGF, which are caused by genetic deficiency or overexpression of particular gene<sup>13</sup>. For example, as genetic variations in very low density lipoprotein receptor (VLDLR) are significantly associated with AMD in humans<sup>28</sup>, transgenic mouse models with VLDLR knockout were established, which demonstrated characteristic features of CNV with the mixed of dry and neovascular forms<sup>29,30</sup>.

The dominant feature of laser induced CNV models are based on laser induction of Bruchs membrane breaking and the injury of the outer retina, leading to the increased expression of pro-angiogenic factors and results in CNV formation<sup>19</sup>. Laser induced CNV model have been applied on rat, mouse, rabbit, pig, and primate<sup>11-13</sup>. The laser-induced CNV model has become one of the standard models in the field of CNV research, such as the predicting of therapeutic value of anti-VEGF therapies<sup>31,32</sup>. In an earlier study, histopathologic evidence of the breaks in Bruch's membrane with fibrovascular growths in subretinal space was found in laser induced rabbit CNV model, an intermediate laser-induced CNV model between rodents and primates, and the characteristic findings in FFA was also demonstrated. But the typical features of rabbit CNV model were vanished within 1 week, leaving only the flat staining lesions in angiography<sup>33</sup>. The rabbit circumvents the cost and ethical issues of the primate, although, the rabbit lacks the key anatomic structure of macula. In Kiilgaard's research<sup>34</sup>, laser induced CNV in pigs occurred on day 7, with the highest incidence of 83% on day 21. The pig eye is approximately as the human eye in size. Like the rabbit, the pig is more convenient in relation to the cost and ethical issues. However, the pig lacks the advantages of high throughput, short duration experiments as available in rat and mouse models of laser induced CNV. In mouse CNV model, CNV reached the maximum area on day 7, which could be visualized and quantified by FFA and immunohistochemical staining techniques<sup>35,36</sup>. After day 7, it started to regress and almost completely disappeared within 35 days post laser, leaving only fibrous tissue<sup>36</sup>. In Cui's research, laser induced CNV of rat appeared on day 7 after treatment, reached the peak at day 21 (84%), and remained stable at day 21 to day 56<sup>37</sup>. Advantages of rodent CNV model include that the model is inexpensive, reproducible, and relatively simple to create. What's more, CNV model in rodent could be done in short time frames. Disadvantages include the small size of the rat/mouse eye compared to the human eye, mice and rats also do not have a macula. Nevertheless, the rat/mouse laser model of CNV is the standard animal model of CNV for most therapeutic exploration experiments currently.

Laser induced monkey CNV model normally developed at 2 weeks post photocoagulation, its success rate of modeling was maintained at 42 to 66.7% from 2 to 7 weeks after laser treatment<sup>38,39</sup>. According to Lin's research<sup>38</sup>, the natural course of monkey CNV may considerably different among individuals, some of them regressed within 2-4 weeks, while others remained stable for more than 20 weeks. Furthermore, the success rate of monkey CNV modeling may also be influenced by the anatomical location of photocoagulation, that is, a higher incidence occurred in macular region compared with outside macular region. In Shen's research, 72% of monkey CNV lesions within the macula area took the form of fluorescein leakage, compared with 12% outside the macula region<sup>40</sup>. In microscopic structures, CNV membranes outside the macula containing fewer new vessels, embedded in firmly packed fibrous tissue may be the latent course, compared with the CNV inside macula<sup>40</sup>. Shen's research revealed that 2-3 weeks post treatment, monkey CNV appeared in 46.4% of 766 laser spots delivered to 58 eyes, and part of the laser spots with fluorescein leakage at 2 weeks remained leaky at 12 weeks post laser treatment<sup>41</sup>. Although CNV on monkey is an ideal animal model, include the close approximation of the monkey retina and macula to the human, size of the primate eye for drug delivery studies, and utility of the model for development of human clinical trials (such as for PDT and anti-angiogenics)<sup>13</sup>, it has limitations, including the limited location (macular area has higher success rate), limited availability, high cost of the animals/animal care/ husbandry, length of experiments and ethical issues regarding use of primates compared with rodents (mice and rats).

An ideal animal model for biological research should possess essential features, including high genetic similarity and analogous pathobiology to humans, low cost, and fewer restrictions. Studies have shown that tree shrews are phylogenetically closer to primates<sup>42,43</sup>. In overall expression patterns in tissues and pathways, tree shrews are more similar to primates than to mice at the tissue-transcriptome level<sup>44</sup>. The tree shrew genome encompasses the orthologues of almost all the 209 known visually related human genes, but lacks two cone photoreceptors, the middle wave-length sensitive proteins<sup>42</sup>, which is consistent with the fact that tree shrews lack the green pigment and possess dichromats<sup>45</sup>. Tree shrews have no specialization or differentiation of a central foveal region. Histologic sections revealed relatively short and thick cones distributed uniformly throughout the retina of tree shrew. The photoreceptors of the tree shrew are mainly composed by cones, rods comprising less than 4% of the total photoreceptors<sup>46</sup>. The two cone types in this animal are specially sensitive to the light at wavelengths of 556nm and 444nm has been determined by ERG flicker photometry<sup>46</sup>. The special constitution of tree shrew photoreceptor is in

general accord with the tree shrew's diurnal habits as well as its great reliance on photopic vision and its visually guided behavior<sup>47</sup>, which is closely resemble to the structure and function of macula lutea of human, and experimental animal model of fundus disease in tree shrew may be able to mimic humans pathological conditions more precisely. Since the tree shrew's retina has similar structure of human's macula, it provides wider location for modeling. The laser spots were placed around the optic disc in this study. FFA and ICGA were used to evaluate the successful rate of CNV modeling in tree shrews (Fig. 3). The leakage appeared in lesions on day 7 (46%), the leakage rate and total area of fluorescent leakage reached the peak on day 21 (70%), and gradually decreased after day 21, proven by FFA. CNV model in tree shrew could be established by krypton laser photocoagulation with high success rate, and reached a maximum success rate of 70%.

SD-OCT is a non-contacted biomedical imaging techniques with high-resolution, which could show the structure of retina and choroid clearly. OCT has been applied for the detection and follow-up for fundus diseases. Longitudinal SD-OCT analysis at various time points gives more information of CNV lesion in animal model instead of relying on FFA only. In the OCT scan images of normal tree shrews, the construction of retina and choroid were clearly demonstrated, which were similar to human. In SD-OCT scans, tree shrews CNV lesions manifested as high reflective mass beneath neural retina, emerging from the breakage of RPE-choriocapillaris complex. In monkey model, CNV lesions were also showed as subretinal hyper-reflective material in SD-OCT<sup>39,48</sup>. Symantas et al recently proposed that SD-OCT provides a detailed CNV pathology within retinal tissue. SD-OCT images of CNV formation, liquid accumulation, and scarring tissue on mouse CNV model were displayed in his research<sup>49</sup>. In our study, liquid accumulation was not observed in the SD-OCT of tree shrew CNV lesions (Fig. 6). However, subretinal space appeared in CNV pathological sections may be caused by the leakage of new blood vessels (Fig. 9). Compared to SD-OCT images of mouse model, the bulging high-reflection lesions on tree shrew were more visible. These findings in SD-OCT not only had similarities with other kind of CNV animal models including rats and monkeys, but also to human CNV caused by myopic CNV<sup>2</sup> and AMD<sup>50</sup>.

Currently, F-VEP is mainly used to monitor the function of optic nerve and visual pathway in ophthalmology. It has been applied on the research of optic neuritis, ischemic optic neuropathy, and other optic neuropathy. F-VEP waveform of healthy mouse is mainly composed of N1, P1, N2 and P2<sup>51</sup>. In the experimental autoimmune optic neuritis on mouse, F-VEP examination manifested as the prolonged latency of P2 and the reduced amplitude of N2-P2<sup>51</sup>. In the rat model of anterior ischemic optic neuropathy, the latency of P2 was also prolonged, with the amplitude decreased<sup>52</sup>. In this study, F-VEP in healthy tree shrew is mainly constructed by N1, P1 and N2. Compared with the normal group, the amplitude of variety of waves reduced in different experimental group, and significantly reduced N1-P1 amplitude was the common performance in experimental groups (Fig. 7). Laser photocoagulation and laser-induced CNV formation jointly triggered the structural and functional impairment of retina may be the underlying cause, which is one of the key components in visual pathway.

The structure of CNV could be also observed in pathological section. Human CNV in pathological section are presented as the rupture of Bruch membrane, neovascularization under retina, migration and proliferation of RPE cells, loss of photoreceptors, and the deposition of macrophages/activated microglia<sup>25</sup>. In this study, the structure of normal retina, choroid and sclera of tree shrew were also showed by pathological sections clearly (Fig. 9), which was similar to human. In tree shrew CNV, newly developed blood capillary, as well as a large number of red blood cells in the lumen were visible at high magnification. RPE cells and inflammatory cells such as pigmented macrophage and small lymphocyte infiltrated into the CNV region were also observed, which were almost similar to human (Fig. 10). In laser-induced CNV model of rat, similar pathological features could also be seen in pathological sections<sup>53,54</sup>. In addition, resident phagocytic cells and microglial cells in the retina translocated into subretinal space and accumulated near the RPE layer were also observed in human CNV<sup>55</sup>. In this study, we have only observed the infiltration of pigment cells, pigmentary macrophage, and small lymphocyte in tree shrew CNV lesions. In addition, CNV in tree shrew was observed at 7 days after photocoagulation, and the relative height of CNV peaked at 14 days after photocoagulation (Fig. 11). However, the relative height of laser induced rat CNV reached its peak and remain stable at 21 days after photocoagulation, which was later than tree shrew<sup>37</sup>.

The homeostasis of vascular system was regulated by a variety of angiogenesis related factors, the imbalance of expression and function of angiogenic factors and angiogenesis inhibitors was one of the major cause of intraocular neovascular disorders. Several studies had shown that, the expression changes of VEGF family<sup>56-58</sup>, Tie-2 system<sup>59-61</sup>, MMP family<sup>18,62,63</sup>, and other factors such as bFGF<sup>64,65</sup> were all associated with CNV development. Whereas, the biological action of transforming growth factor (TGF- $\beta$ )<sup>66,67</sup> and PEDF<sup>68-70</sup> mainly focused on the inhibition of angiogenesis, and their down-regulation also related to pathological vascular formation. In this study, the mRNA expression of VEGF-A, VEGF-B, Ang-1, Ang-2, MMP-2, MMP-9, MMP-13, bFGF and PLGF are significantly increased in experimental groups. Whereas, the expression of TGF- $\beta$  and PEDF are significantly decreased (Fig. 12,13). The expression disorder of those factors may have participated in the process of tree shrew CNV formation.

## Conclusion

Krypton laser photocoagulation could successfully induce the CNV model on tree shrew with high success rate. Typical CNV formation has been proven by FFA/ICGA, OCT, histological finding and expression change of angiogenesis related factors. Tree shrew CNV model is reproducible, cost-effective, and relatively simple to establish with short experimental duration, may be used as an ideal animal model for CNV research, such as therapeutic intervention studies.

## Declarations

### Acknowledgments

The authors would like to acknowledge Min Wu, MD for her assistance on experimental design, editing of the final manuscript and Zhi-chao Sheng for the clinical data. We would also like to acknowledge support from the Yunnan Eye Disease Clinical Medical Center, Yunnan Eye Disease Clinical Medical Research

Center, Kunming, China.

### Author contributions

W.M conceived the experiment and edited manuscript. L.XC conducted the experiment, analyzed data and wrote the main manuscript text. All authors reviewed the manuscript.

### Competing interests

The authors declare no competing interests.

### Data availability statement

The datasets used to support the findings of this study are available from the corresponding author upon request.

## References

- 1 Jin, K. *et al.* Multimodal deep learning with feature level fusion for identification of choroidal neovascularization activity in age-related macular degeneration. *Acta Ophthalmol***100**, e512-e520 (2022).
- 2 Shi, X. *et al.* Presence or absence of choroidal hyper-transmission by SD-OCT imaging distinguishes inflammatory from neovascular lesions in myopic eyes. *Graefes Arch Clin Exp Ophthalmol***258**, 751-758 (2020).
- 3 Richey, B. F. *et al.* SMOKING, RURAL RESIDENCE AND DIABETES AS RISK FACTORS FOR PRESUMED OCULAR HISTOPLASMOSIS SYNDROME. *Retina***42**, 369-374 (2022).
- 4 Ehrenberg, M. & Benny, O. Evolving multidimensional pharmacological approaches to CNV therapy in AMD. *Current Eye Research*, 1 (2017).
- 5 Mi, L., Chen, L., Liu, B., Wen, F. & Zhang, X. Long-Term Natural Outcomes of Simple Hemorrhage Associated with Lacquer Crack in High Myopia: A Risk Factor for Myopic CNV? *Journal of ophthalmology***2018**, 1-7 (2018).
- 6 Budzinskaya, M. V. & Plyukhova, A. A. [Differential diagnosis of various types of fluids on the eye fundus in patients with age-related macular degeneration]. *Vestn Oftalmo***136**, 354-358 (2020).
- 7 Khurana, R. N., Hill, L., Ghanekar, A. & Gune, S. Agreement of Spectral-Domain OCT with Fluorescein Leakage in Neovascular Age-Related Macular Degeneration: Post Hoc Analysis of the HARBOR Study. *Ophthalmol Retina* (2020).
- 8 Chakravarthy, U. *et al.* Progression from Early/Intermediate to Advanced Forms of Age-Related Macular Degeneration in a Large UK Cohort: Rates and Risk Factors. *Ophthalmol Retina***4**, 662-672 (2020).
- 9 Archer, D. B. & Gardiner, T. A. Morphologic fluorescein angiographic, and light microscopic features of experimental choroidal neovascularization. *American journal of ophthalmology***91**, 297-311 (1981).
- 10 Cui, J., Liu, Y., Zhang, J. & Yan, H. An experimental study on choroidal neovascularization induced by Krypton laser in rat model. *Photomedicine & Laser Surgery***32**, 30 (2014).
- 11 Dobi, E. T., Puliafito, C. A. & Destro, M. A new model of experimental choroidal neovascularization in the rat. *Arch Ophthalmol***107**, 264-269 (1989).
- 12 Tobe, T. *et al.* Targeted disruption of the FGF2 gene does not prevent choroidal neovascularization in a murine model. *Am J Pathol***153**, 1641-1646 (1998).
- 13 Grossniklaus, H. E., Kang, S. J. & Berglin, L. Animal models of choroidal and retinal neovascularization. *Prog Retin Eye Res***29**, 500-519 (2010).
- 14 Yao, Y. G. Creating animal models, why not use the Chinese tree shrew (*Tupaia belangeri chinensis*)? *Zool Res***38**, 118-126 (2017).
- 15 Xiao, J., Liu, R. & Chen, C. S. Tree shrew (*Tupaia belangeri*) as a novel laboratory disease animal model. *Zool Res***38**, 127-137 (2017).
- 16 Levy, A. M., Fazio, M. A. & Grytz, R. Experimental myopia increases and scleral crosslinking using genipin inhibits cyclic softening in the tree shrew sclera. *Ophthalmic Physiol Opt***38**, 246-256 (2018).
- 17 Guo, L., Frost, M. R., Siegwart, J. T. & Norton, T. T. Gene expression signatures in tree shrew sclera during recovery from minus-lens wear and during plus-lens wear. *Mol Vis***25**, 311-328 (2019).
- 18 Lambert, V. *et al.* Matrix metalloproteinase-9 contributes to choroidal neovascularization. *Am J Pathol***161**, 1247-1253 (2002).
- 19 Montezuma, S. R., Vavvas, D. & Miller, J. W. Review of the ocular angiogenesis animal models. *Semin Ophthalmol***24**, 52-61 (2009).
- 20 Spilsbury, K., Garrett, K. L., Shen, W. Y., Constable, I. J. & Rakoczy, P. E. Overexpression of vascular endothelial growth factor (VEGF) in the retinal pigment epithelium leads to the development of choroidal neovascularization. *Am J Pathol***157**, 135-144 (2000).

- 21 Zahn, G. *et al.* Preclinical evaluation of the novel small-molecule integrin alpha5beta1 inhibitor JSM6427 in monkey and rabbit models of choroidal neovascularization. *Arch Ophthalmol***127**, 1329-1335 (2009).
- 22 Qiu, G. *et al.* A new model of experimental subretinal neovascularization in the rabbit. *Exp Eye Res***83**, 141-152 (2006).
- 23 Li, Y. *et al.* Real-time OCT guidance and multimodal imaging monitoring of subretinal injection induced choroidal neovascularization in rabbit eyes. *Exp Eye Res***186**, 107714 (2019).
- 24 Lima, L. H., Farah, M. E., Gum, G., Ko, P. & de Carvalho, R. A. P. Sustained and targeted episcleral delivery of celecoxib in a rabbit model of retinal and choroidal neovascularization. *Int J Retina Vitreous***4**, 31 (2018).
- 25 Liu, S. *et al.* A new rat model of treatment-naive quiescent choroidal neovascularization induced by human VEGF165 overexpression. *Biol Open***9** (2020).
- 26 Kokki, E., Karttunen, T., Olsson, V., Kinnunen, K. & Yli-Herttua, S. Human Vascular Endothelial Growth Factor A165 Expression Induces the Mouse Model of Neovascular Age-Related Macular Degeneration. *Genes (Basel)***9** (2018).
- 27 Cao, J. *et al.* A subretinal matrigel rat choroidal neovascularization (CNV) model and inhibition of CNV and associated inflammation and fibrosis by VEGF trap. *Invest Ophthalmol Vis Sci***51**, 6009-6017 (2010).
- 28 Haines, J. L. *et al.* Functional candidate genes in age-related macular degeneration: significant association with VEGF, VLDLR, and LRP6. *Invest Ophthalmol Vis Sci***47**, 329-335 (2006).
- 29 Hu, W. *et al.* Expression of VLDLR in the retina and evolution of subretinal neovascularization in the knockout mouse model's retinal angiomatous proliferation. *Invest Ophthalmol Vis Sci***49**, 407-415 (2008).
- 30 Heckenlively, J. R. *et al.* Mouse model of subretinal neovascularization with choroidal anastomosis. *Retina***23**, 518-522 (2003).
- 31 Krzystolik, M. G. *et al.* Prevention of experimental choroidal neovascularization with intravitreal anti-vascular endothelial growth factor antibody fragment. *Arch Ophthalmol***120**, 338-346 (2002).
- 32 Ji, W. W. *et al.* Recombinant humanized anti-vascular endothelial growth factor monoclonal antibody efficiently suppresses laser-induced choroidal neovascularization in rhesus monkeys. *Eur J Pharm Sci***109**, 624-630 (2017).
- 33 elDirini, A. A., Ogden, T. E. & Ryan, S. J. Subretinal endophotocoagulation. A new model of subretinal neovascularization in the rabbit. *Retina***11**, 244-249 (1991).
- 34 Kiilgaard, J. F. *et al.* A new animal model of choroidal neovascularization. *Acta Ophthalmol Scand***83**, 697-704 (2005).
- 35 Gong, Y. *et al.* Optimization of an Image-Guided Laser-Induced Choroidal Neovascularization Model in Mice. *PLoS One***10**, e0132643 (2015).
- 36 Ishikawa, K., Kannan, R. & Hinton, D. R. Molecular mechanisms of subretinal fibrosis in age-related macular degeneration. *Exp Eye Res***142**, 19-25 (2016).
- 37 Cui, J., Liu, Y., Zhang, J. & Yan, H. An experimental study on choroidal neovascularization induced by Krypton laser in rat model. *Photomed Laser Surg***32**, 30-36 (2014).
- 38 Lin, X., Wang, Q. & He, M. Repeated retinal photocoagulation in monkeys for the optimization of a laser-induced choroidal neovascularization model. *Exp Eye Res***184**, 1-7 (2019).
- 39 Inagaki, S. *et al.* Anti-vascular endothelial growth factor antibody limits vascular leakage and decreases subretinal fibrosis in a cynomolgus monkey choroidal neovascularization model. *Curr Neurovasc Res* (2020).
- 40 Shen, W. Y. *et al.* Predilection of the macular region to high incidence of choroidal neovascularization after intense laser photocoagulation in the monkey. *Arch Ophthalmol***122**, 353-360 (2004).
- 41 Shen, W. Y., Yu, M. J., Barry, C. J., Constable, I. J. & Rakoczy, P. E. Expression of cell adhesion molecules and vascular endothelial growth factor in experimental choroidal neovascularisation in the rat. *Br J Ophthalmol***82**, 1063-1071 (1998).
- 42 Fan, Y. *et al.* Genome of the Chinese tree shrew. *Nat Commun***4**, 1426 (2013).
- 43 Fan, Y. *et al.* Chromosomal level assembly and population sequencing of the Chinese tree shrew genome. *Zool Res***40**, 506-521 (2019).
- 44 Ye, M. S. *et al.* Comprehensive annotation of the Chinese tree shrew genome by large-scale RNA sequencing and long-read isoform sequencing. *Zool Res***42**, 692-709 (2021).
- 45 Hunt, D. M. *et al.* Molecular evolution of trichromacy in primates. *Vision Res***38**, 3299-3306 (1998).
- 46 Jacobs, G. H. & Neitz, J. Spectral mechanisms and color vision in the tree shrew (*Tupaia belangeri*). *Vision Res***26**, 291-298 (1986).
- 47 Samorajski, T., Ordy, J. M. & Keefe, J. R. Structural organization of the retina in the tree shrew (*Tupaia glis*). *J Cell Biol***28**, 489-504 (1966).

- 48 Olvera-Montano, O. *et al.* Comparing The Efficacy Of An Anti-Human VEGF-A Neutralizing Antibody Versus Bevacizumab On A Laser-Induced Choroidal Neovascularization (CNV) Rhesus Monkey Model. *Drug Des Devel Ther***13**, 3813-3821 (2019).
- 49 Ragauskas, S., Kielczewski, E., Vance, J., Kaja, S. & Kalesnykas, G. In Vivo Multimodal Imaging and Analysis of Mouse Laser-Induced Choroidal Neovascularization Model. *J Vis Exp* (2018).
- 50 Book, B. *et al.* [Visual acuity in anti-VEGF therapy for AMD : Can specific characteristics in the SD-OCT help?]. *Ophthalmology***114**, 49-56 (2017).
- 51 Liu, Y., You, C., Zhang, Z., Zhang, J. & Yan, H. Roles of Treg/Th17 Cell Imbalance and Neuronal Damage in the Visual Dysfunction Observed in Experimental Autoimmune Optic Neuritis Chronologically. *Neuromolecular Med***17**, 391-403 (2015).
- 52 Wang, R. S. *et al.* Establishing an experimental model of photodynamically induced anterior ischemic optic neuropathy. *Vis Neurosci***28**, 155-162 (2011).
- 53 Eter, N. *et al.* In vivo visualization of dendritic cells, macrophages, and microglial cells responding to laser-induced damage in the fundus of the eye. *Investigative Ophthalmology & Visual Science***49**, 3649 (2008).
- 54 Sakurai, E., Anand, A., Ambati, B. K., Van, R. N. & Ambati, J. Macrophage depletion inhibits experimental choroidal neovascularization. *Investigative Ophthalmology & Visual Science***44**, 3578-3585 (2003).
- 55 Combadière, C. *et al.* CX3CR1-dependent subretinal microglia cell accumulation is associated with cardinal features of age-related macular degeneration. *Journal of Clinical Investigation***117**, 2920 (2007).
- 56 Ferrara, N., Gerber, H. P. & Lecouter, J. The biology of VEGF and its receptors. *Nature medicine***9**, 669-676 (2003).
- 57 Mammadzada, P., Gudmundsson, J., Kvant, A. & André, H. Differential hypoxic response of human choroidal and retinal endothelial cells proposes tissue heterogeneity of ocular angiogenesis. *Acta ophthalmologica***94**, 805-814 (2016).
- 58 Robinson, C. J. & Stringer, S. E. The splice variants of vascular endothelial growth factor (VEGF) and their receptors. *Journal of Cell Science***114**, 853 (2001).
- 59 Puri, M. C., Rossant, J., Alitalo, K., Bernstein, A. & Partanen, J. The receptor tyrosine kinase TIE is required for integrity and survival of vascular endothelial cells. *Embo J***14**, 5884-5891 (1995).
- 60 Asahara, T. *et al.* Tie2 receptor ligands, angiotensin-1 and angiotensin-2, modulate VEGF-induced postnatal neovascularization. *Circ Res***83**, 233-240 (1998).
- 61 Augustin, H. G., Koh, G. Y., Thurston, G. & Alitalo, K. Control of vascular morphogenesis and homeostasis through the angiotensin-Tie system. *Nat Rev Mol Cell Biol***10**, 165-177 (2009).
- 62 Xu, J. *et al.* Over-expression of BMP4 inhibits experimental choroidal neovascularization by modulating VEGF and MMP-9. *Angiogenesis***15**, 213-227 (2012).
- 63 Lambert, V. *et al.* MMP-2 and MMP-9 synergize in promoting choroidal neovascularization. *Faseb J***17**, 2290-2292 (2003).
- 64 Abdel-Rahman, M. H. *et al.* Investigation of the potential utility of a linomide analogue for treatment of choroidal neovascularization. *Experimental eye research***91**, 837-843 (2010).
- 65 Hu, W. *et al.* Differences in the temporal expression of regulatory growth factors during choroidal neovascular development. *Experimental eye research***88**, 79 (2009).
- 66 Jakobsson, L. & Meeteren, L. A. V. Transforming growth factor  $\beta$  family members in regulation of vascular function: In the light of vascular conditional knockouts. *Experimental Cell Research***319**, 1264-1270 (2013).
- 67 Schlecht, A. *et al.* Deletion of Endothelial TGF- $\beta$  Signaling Leads to Choroidal Neovascularization. *American Journal of Pathology* (2017).
- 68 Tong, J. P. & Yao, Y. F. Contribution of VEGF and PEDF to choroidal angiogenesis: a need for balanced expressions. *Clinical Biochemistry***39**, 267-276 (2006).
- 69 Sarojini, H. *et al.* PEDF from mouse mesenchymal stem cell secretome attracts fibroblasts. *Journal of Cellular Biochemistry***104**, 1793 (2008).
- 70 Yu, Y. J. *et al.* Inhibition of choroidal neovascularization by lentivirus-mediated PEDF gene transfer in rats. *International Journal of Ophthalmology***9**, 1112-1120 (2016).

## Figures

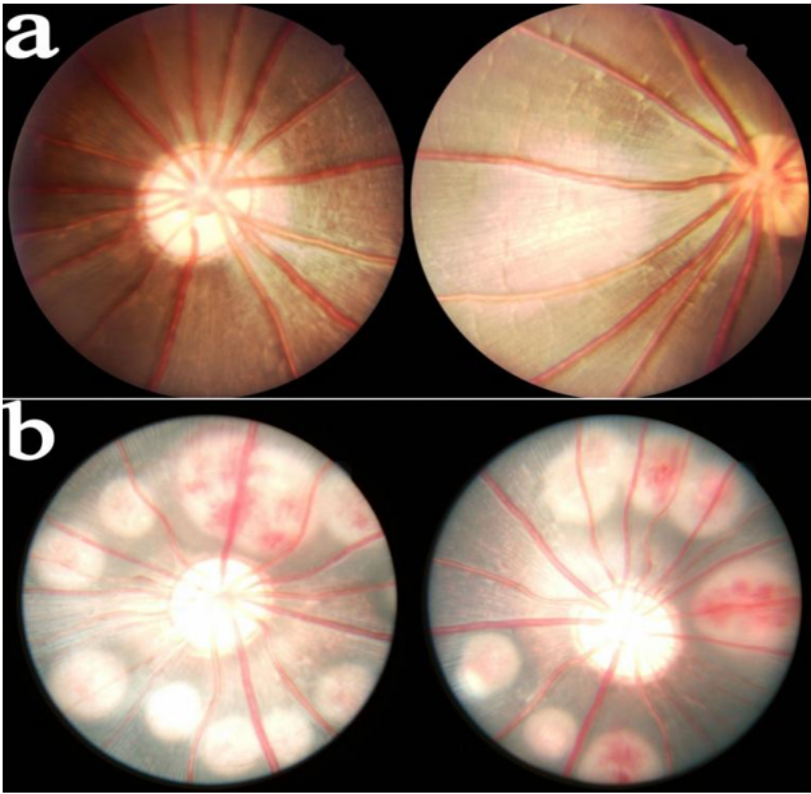


Figure 1

Fundus photography

a. fundus photography of healthy tree shrew b. fundus photography after photocoagulation

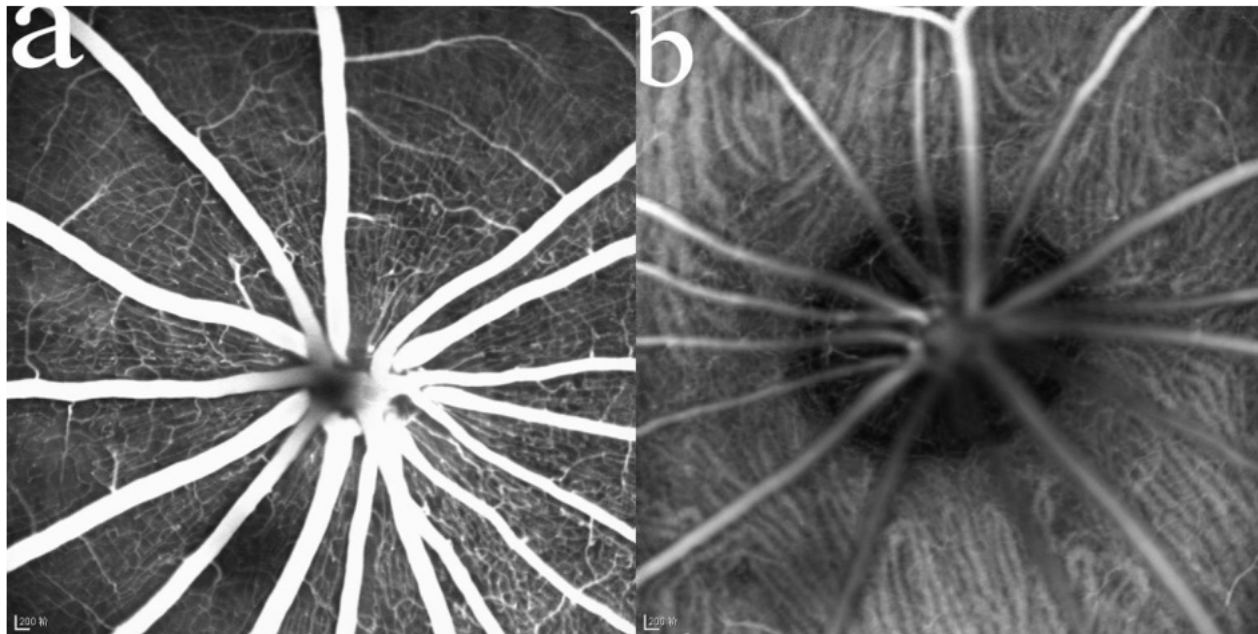
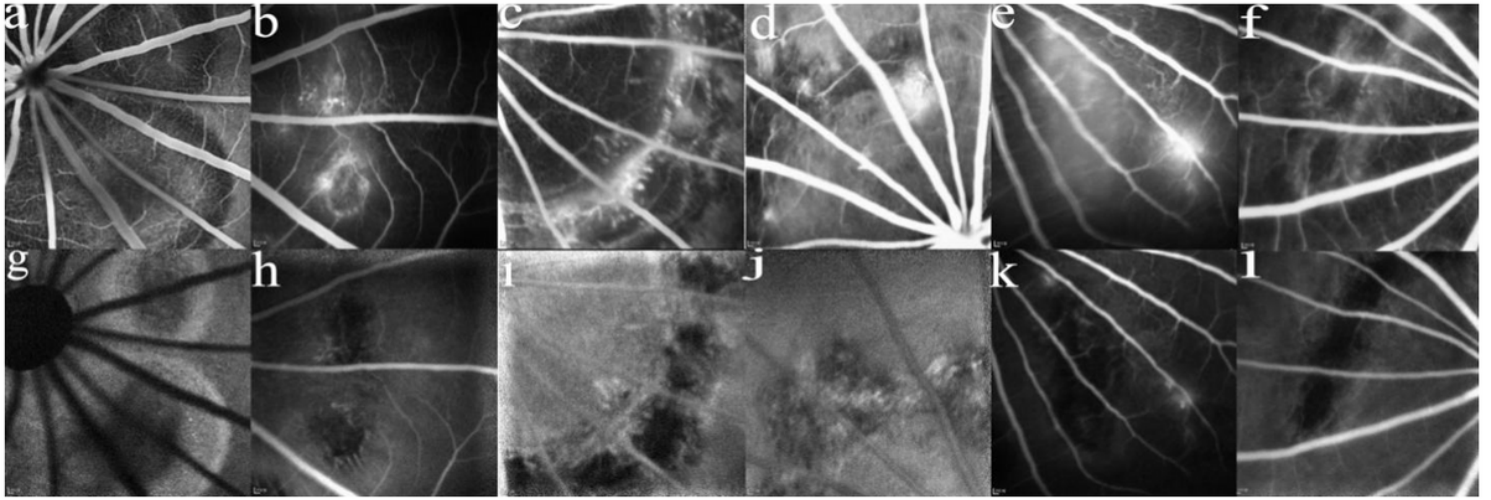


Figure 2

FFA/ICGA of healthy tree shrew

a. FFA of healthy tree shrew b. ICGA of healthy tree shrew



**Figure 3**  
 FFA/ICGA of tree shrew CNV  
 a. FFA showed that pieces of low background fluorescence presented at laser spot 3 days post laser; b-e. tree shrew CNV was revealed by fluorescence leakage in FFA typical images 7-21 days post laser; f. FFA showed fluorescence leakage vanished, leaving the scar tissue dyed 28 days post laser; g. ICGA showed the clumpy of high fluorescence 3 days post laser; h-k. tree shrew CNV was revealed by mottled strong fluorescence in ICGA 7-21 days post laser; l. strong fluorescence in ICGA disappeared, leaving sheet of low fluorescence behind 28 days post laser.

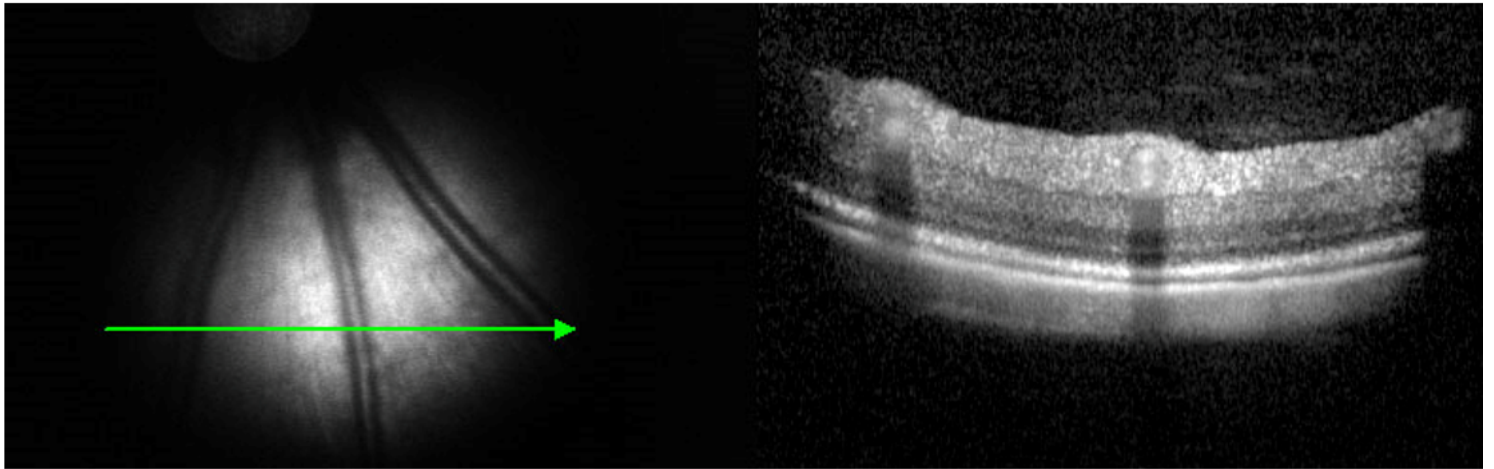


**Figure 4**  
 SD-OCT image of healthy tree shrew

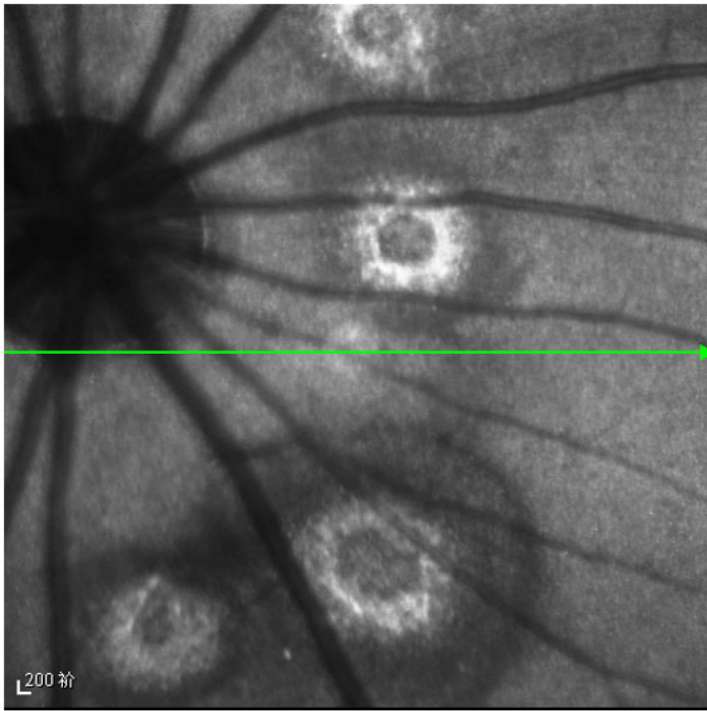


**Figure 5**

Red-free fundus photography after photocoagulation

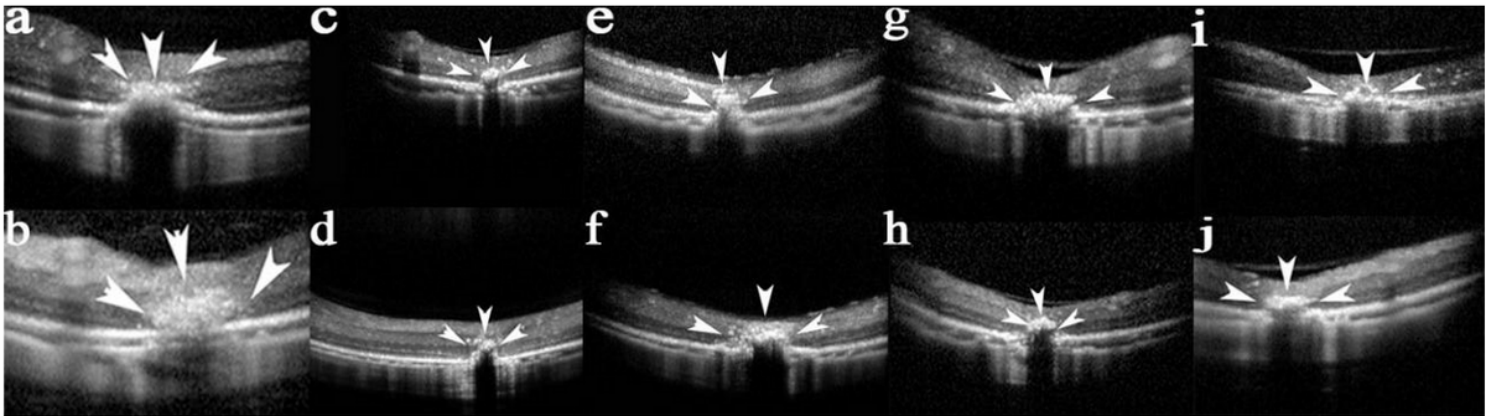


**Figure 6**

SD-OCT image of tree shrew CNV

a-b. at 3 days post laser, interruption of RPE connection, thickening and deformation of RPE and choroidal capillaries appeared; c-d. at 7 days post laser, spindle-shaped, high-reflection region could be seen at laser spot area; e-f. at 14 days post laser, the breadth and height of high-reflection region increased; g-h. at 21 days post laser, scar reflection of retina, RPE and choroid were found; i-j. at 28 days post laser, scar reflection aggravated.

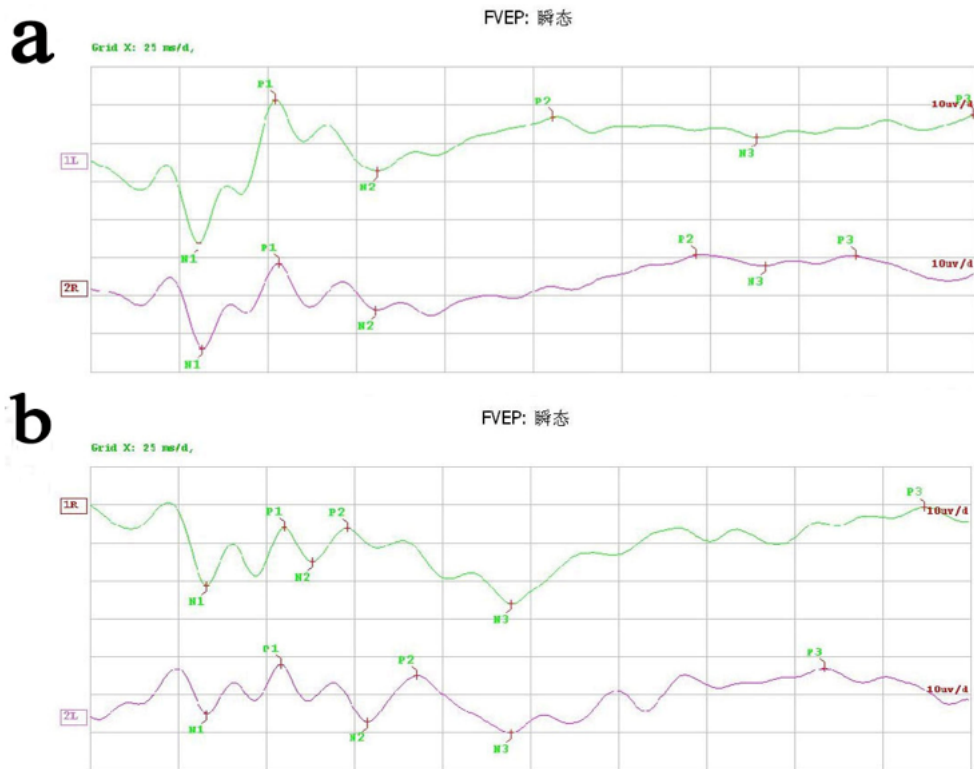


Figure 7

F-VEP images of healthy tree shrew

a-b. F-VEP images of different individuals

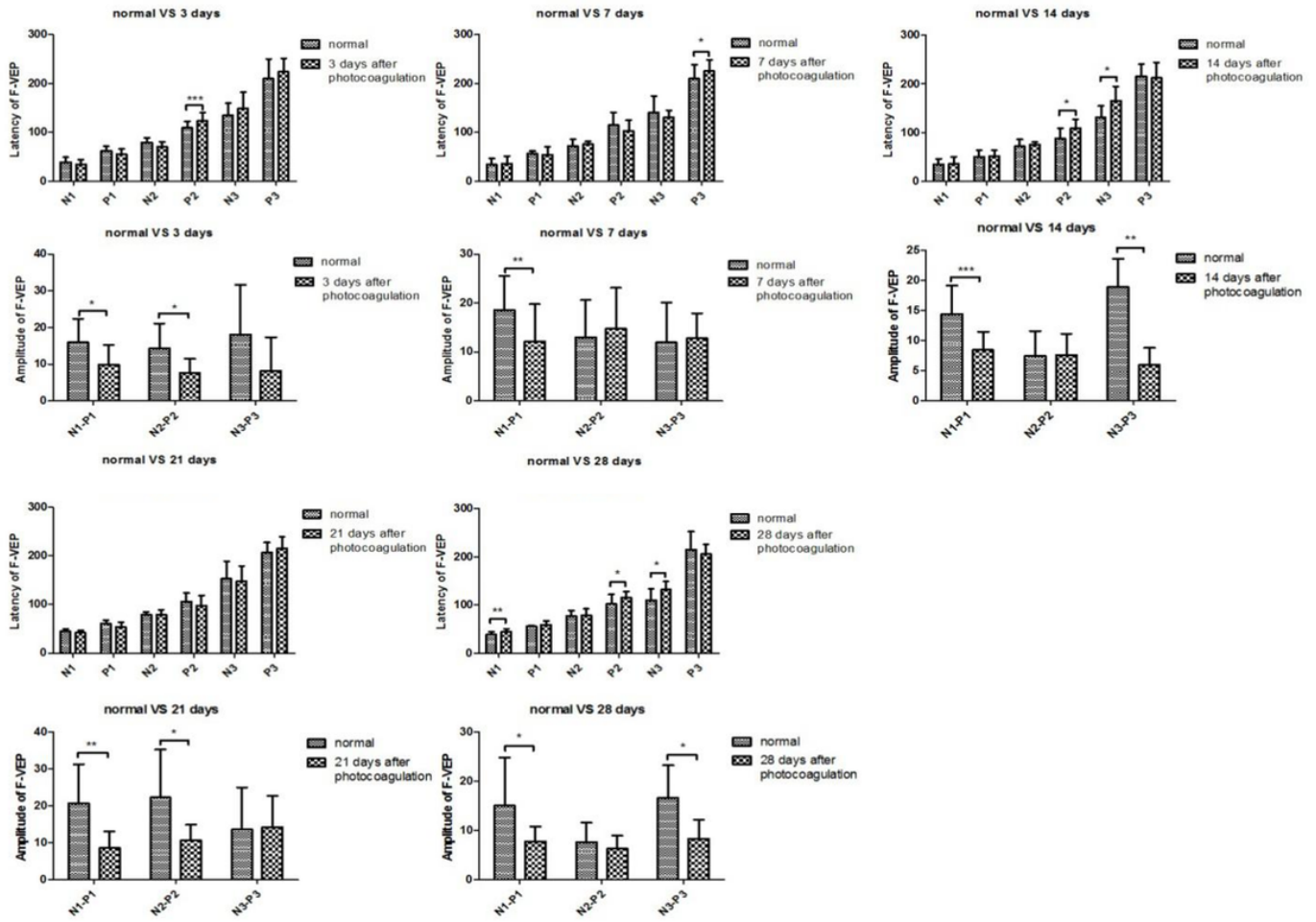


Figure 8

Parameter of F-VEP before and after photocoagulation

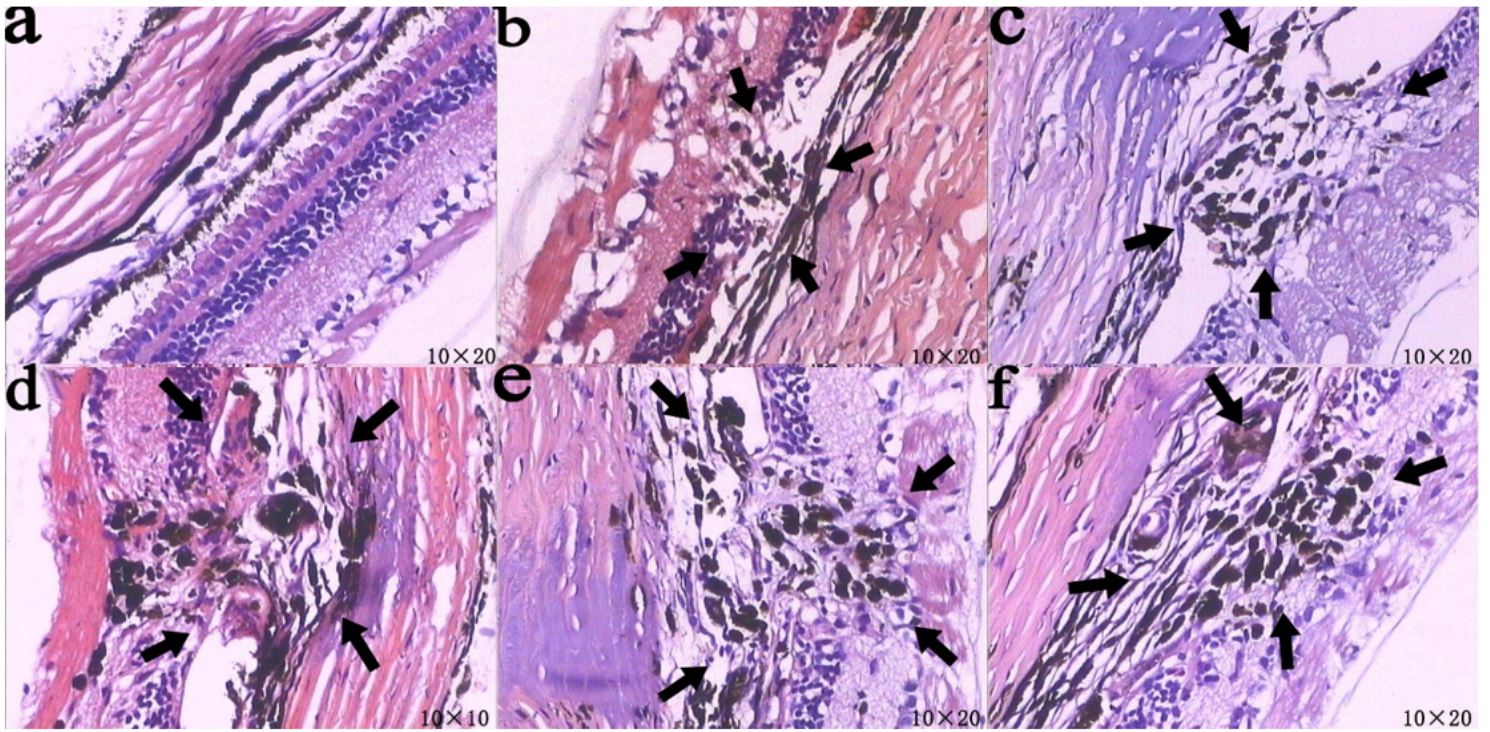


Figure 9

Pathological sections of tree shrew CNV (arrow)

a. pathological sections of posterior segment in healthy tree shrew; b. CNV lesion 3 days post-laser; c. CNV lesion 7 days post-laser; d. CNV lesion 14 days post-laser; e. CNV lesion 21 days post-laser; f. CNV lesion 28 days post-laser.

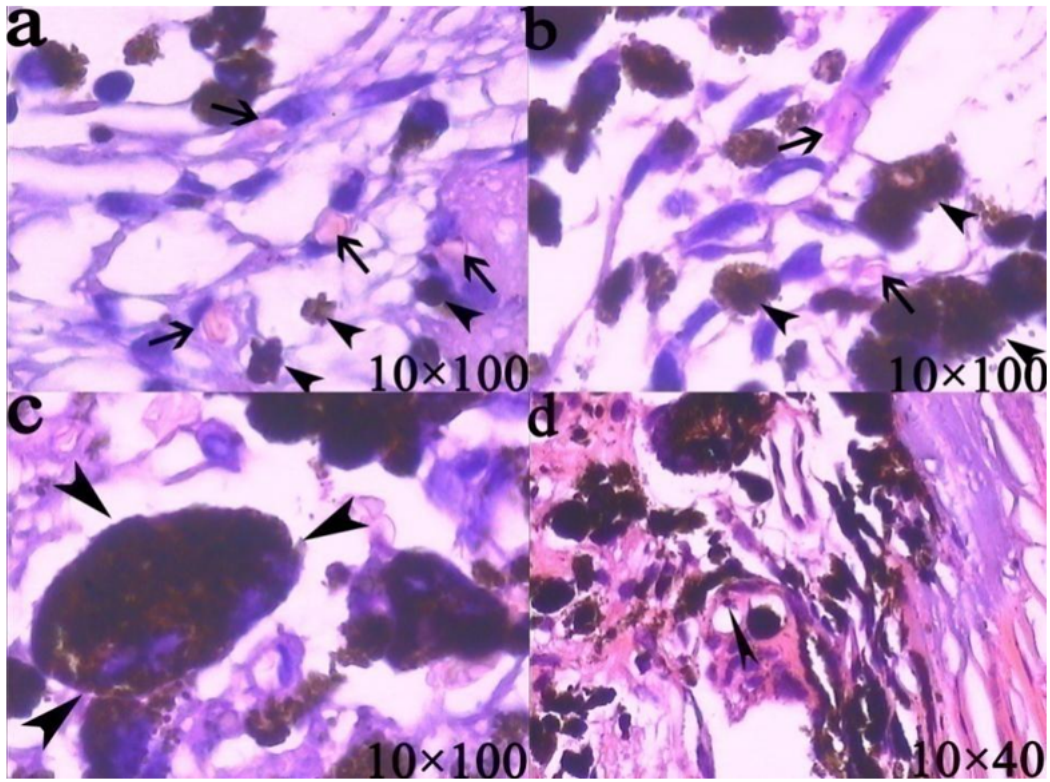


Figure 10

new vessels and inflammatory cells under high magnification

a-b. newly formed thin-walled capillaries with red blood cells in the tube (long arrow), the infiltration of pigment cells (arrow); c. the infiltration of pigmentary macrophage; d. the infiltration of small lymphocyte

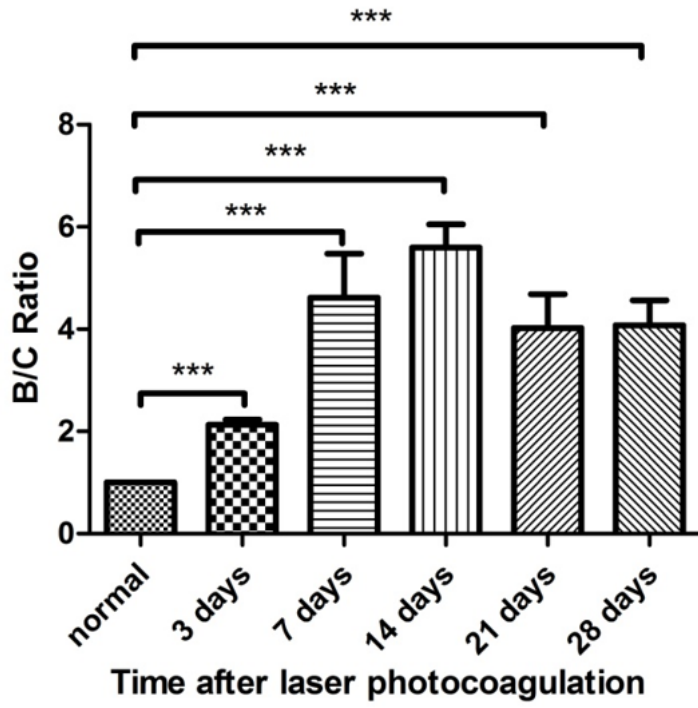


Figure 11

Relative height of CNV in tree shrew

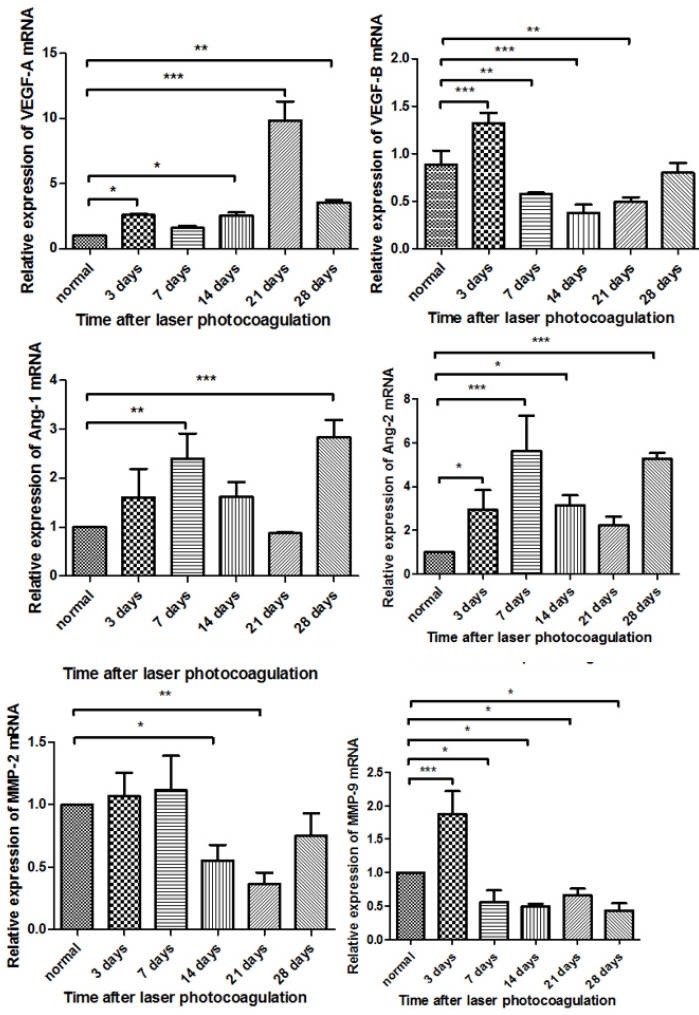


Figure 12

Relative expression of VEGF-A, VEGF-B, Ang-1, Ang-2, MMP-2, MMP-9 mRNA

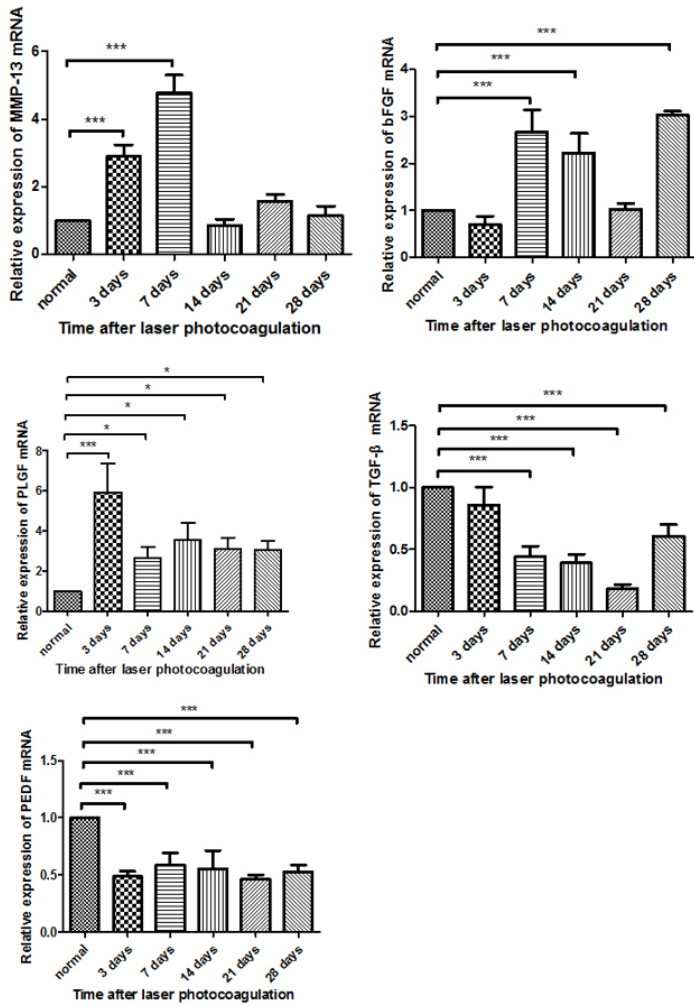


Figure 13

Relative expression of MMP-13, bFGF, PLGF, TGF-β, PEDF mRNA